Load partitioning during compressive loading of a Mg/MgB$_2$ composite

M.L. Young [a], J. DeFouw [a], J.D. Almer [b], D.C. Dunand [a],*

[a] *Department of Materials Science and Engineering, Northwestern University, Evanston, IL 60208, USA*
[b] *Argonne National Laboratory, Argonne, IL 60439, USA*

Abstract

A composite, consisting of 68 vol.% superconducting continuous MgB$_2$ fibers aligned within a ductile Mg matrix, was loaded in uniaxial compression and the volume-averaged lattice strains in the matrix and fiber were measured in situ by synchrotron X-ray diffraction as a function of applied stress. In the elastic range of the composite, both phases exhibit the same strain, indicating that the matrix is transferring load to the fibers according to a simple iso-strain model. In the plastic range of the composite, the matrix is carrying proportionally less load. Plastic load transfer from matrix to fibers is complex due to presence in the fibers of a stiff WB$_4$ core and of cracks produced during the in situ synthesis of the MgB$_2$ fibers from B fibers. Also, load transfer behavior was observed to be different in bulk and near-surface regions, indicating that surface measurements are prone to error.
© 2007 Acta Materialia Inc. Published by Elsevier Ltd. All rights reserved.

Keywords: Metal matrix composites; Internal stresses; Synchrotron radiation; X-ray diffraction; Superconductors

1. Introduction

Magnesium diboride (MgB$_2$) is of interest as a superconductor due to its unusually high transition temperature ($T_c = 39$ K [1]) as compared with other binary intermetallic superconducting compounds, and due to its low material cost, ease of fabrication and lack of weak-link behavior at grain boundaries as compared with oxide superconductors [2–4]. Fabrication of MgB$_2$ tapes and wires by the powder-in-tube (PIT) method has been the topic of numerous studies [5–13]. However, the brittleness of the monolithic MgB$_2$ core within the tube remains an obstacle for applications of PIT tapes and wires. To overcome this problem, composites consisting of numerous aligned MgB$_2$ fibers embedded within a ductile Mg matrix (Mg/MgB$_{2f}$ composites) have been proposed. The composite architecture, where a continuous matrix surrounds each superconducting fiber, improves toughness and crack arrest under mechanical loading as well as heat conductivity

when breakdown in superconductivity occurs locally in some fibers [14]. Such Mg/MgB$_{2f}$ composites can be fabricated by a simple method, where preforms of aligned B fibers are infiltrated and reacted in situ with excess liquid magnesium, which, upon solidification after the end of the reaction, forms the metallic matrix [15,16]. Similar Mg/MgB$_2$ composites, where the MgB$_2$ phase is not in fiber form, have also been reported [15,17–20].

Understanding the mechanical properties of these Mg/MgB$_{2f}$ composites is relevant to their operation in environments where they are subjected to mechanical stresses, e.g. during handling of wires, or during use as windings in electromagnets as a result of the Lorentz forces [21]. The load partitioning occurring between matrix and reinforcement in other metal matrix composites (MMCs) has been the subject of much research: internal phase strain evolution during elastic and plastic deformation has been measured experimentally by neutron [22–27] and synchrotron X-ray [28–32] diffraction, and explained in terms of matrix plasticity, interface damage and reinforcement fracture. Non-destructive imaging of internal damage occurring in composites during loading has also been performed using

---

* Corresponding author. Tel.: +1 847 491 5933; fax: +1 847 491 7820.
E-mail address: dunand@northwestern.edu (D.C. Dunand).

synchrotron X-ray techniques [29,33–37], often in conjunction with strain measurements.

The goal of the present study is to use synchrotron X-ray diffraction to measure phase strains during uniaxial compressive deformation of Mg/MgB_{2f} composites as a function of applied stress. Load transfer between the Mg and MgB_2 main phases, as well as a minority WB_4 phase found at the core of the fibers, is measured for various crystallographic orientations, and results are discussed based on simple rule-of-mixture models. Also, measurements in bulk and near-surface volumes are compared to assess the validity of near-surface measurements using conventional X-rays sources.

2. Experimental procedures

2.1. Composite processing

Fibers of 99.999% pure boron (140 μm in diameter, produced by chemical vapor deposition by Specialty Materials, Inc., Lowell, MA) were cut to 25 mm lengths and aligned at 20% volume fraction within a titanium crucible (8 mm inside diameter, 0.75 mm wall thickness). A billet of 99.95% pure magnesium (from Alfa Aesar, Ward Hill, MA) was positioned above the fibers, and melted by heating the crucible to 800 °C in vacuum. The melt was then infiltrated into the fiber preform by application of argon gas pressurized to 3.2 MPa, using a custom pressure infiltrator [14,15,38]. After cooling to ambient temperature, the titanium crucible containing the solidified Mg/B composite was sealed with a steel cap and heat-treated at 950 °C for 2.5 h to allow for complete reaction of the B fibers with the liquid Mg to form MgB_2 fibers; the air in the sealed crucible reacted with the excess liquid Mg, so no oxygen or nitrogen was present during the reaction.

2.2. Diffraction experiments

A cylindrical sample (5 mm in diameter and 10 mm in height) was machined from the central part of the infiltrated, reacted composite, which displayed a high volume fraction of aligned MgB_2 fibers (unlike the sample circumferential outer layer, which was mostly fiber-free). As shown schematically in Fig. 1, uniaxial compression testing was performed using a custom-built, screw-driven loading system at the 1-ID beam line of the Advanced Photon Source (Argonne National Laboratory, IL), similar to that used in our previous research on other MMCs [28, 30–32,39–42]. Before compression testing, an optical metallography surface image of the composite end and a radiographic transmission image of a full cross-section (5 mm in diameter and 1.02 mm in height, cut from a region immediately adjacent to the Mg/MgB_{2f} sample) were collected, as shown in Fig. 2a and b. The general setup for the imaging mode of the experiment is shown in Fig. 1 and similar to that used in Refs. [43–46]. Compressive load on the composite was applied parallel to the fiber axis and the X-ray beam penetrated the composite perpendicular to the fiber axis. A strain gage affixed to the sample recorded the macroscopic strain values. The stress was increased in steps of ∼30 MPa and held constant during the diffraction measurements. After reaching a maximum compressive value of −520 MPa, the stress was reduced to 0 MPa in steps of ∼100 MPa.

At each stress level, diffraction measurements were collected for 90 s, using a monochromatic 81 keV ($\lambda = 0.015$ nm) X-ray beam with a square 100×100 μm^2 cross-section. Complete Debye–Scherrer diffraction rings from the crystalline phases present in the diffraction volumes were recorded using an image plate (MAR345) positioned at a distance of 1500 mm from the sample, as illustrated in Fig. 1. Additional calibration diffraction rings were produced from a thin layer of pure ceria (CeO_2) powder mixed with vacuum grease, which was smoothly applied to the back face of the composite. The image plate had a 345 mm diameter providing 100 μm pixel size with a 16-bit dynamic range. A typical diffraction pattern of the Mg/MgB_{2f} composite is shown in Fig. 3. For each stress level, diffraction patterns were collected near the center of the sample face by scanning over a 1 mm vertical section, resulting in a total diffracting volume of $0.1 \times 1 \times 5 = 0.5$ mm^3, thus providing an average value for the lattice strains. This volume is illustrated in Fig. 4a, which shows a radiograph near the center of the composite. Also, for each stress level, diffraction patterns were collected from a small volume very close to the surface of the cylindrical sample:
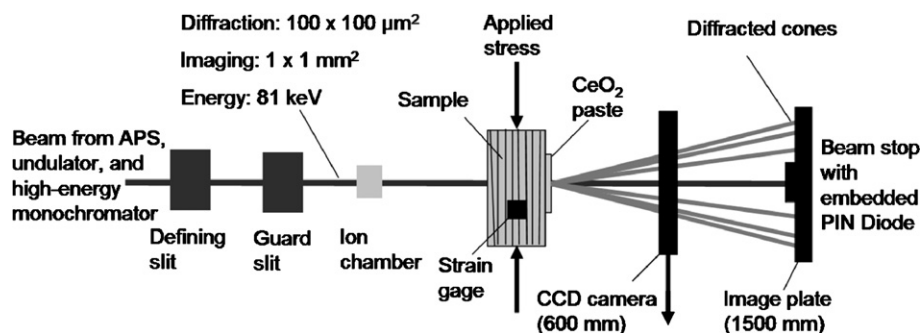

Fig. 1. Schematic of experimental setup for combined diffraction and imaging measurements. For diffraction, the CCD camera is removed.
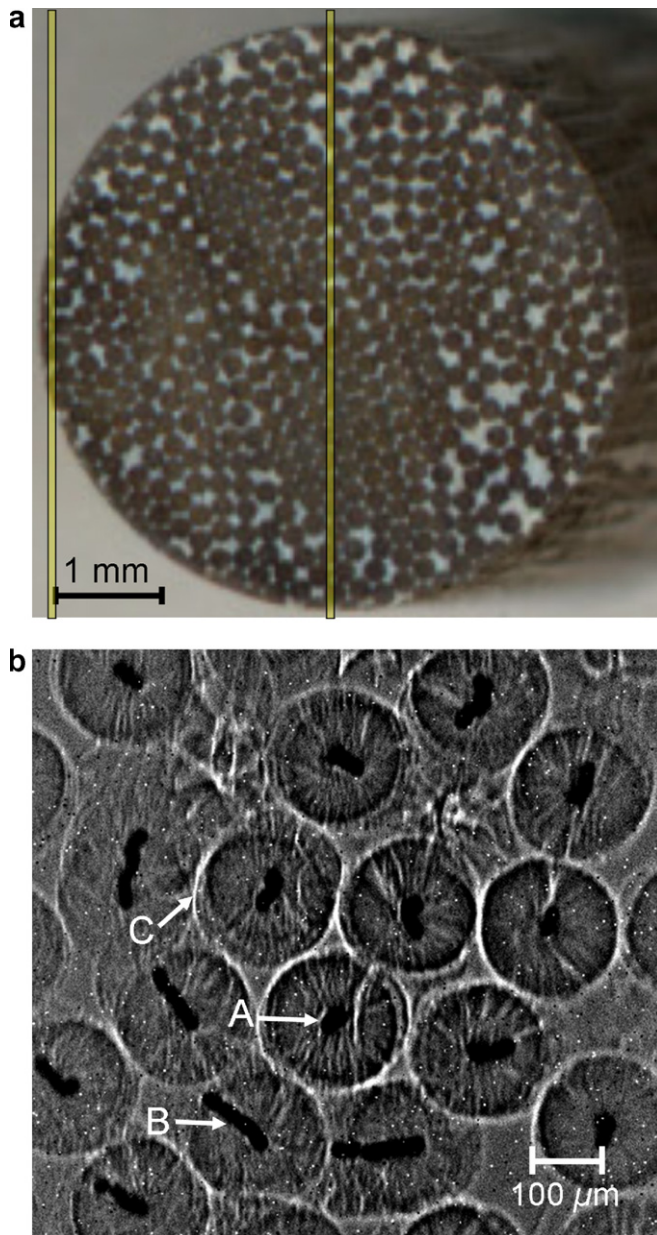
Fig. 2. (a) Optical image of transverse cross-section of Mg/MgB$_{2f}$ composite (the fibers are dark and the matrix is light). The beam path (diffraction volume) is illustrated for bulk and near-surface measurements. (b) Radiographic phase-enhanced image of a 1.02 mm thick transverse cross-section of Mg/MgB$_{2f}$ composite. The lighter regions (C) are the interface between the MgB$_2$ fibers and the Mg matrix. The black regions are the WB$_4$ fiber cores (core A is perpendicular and core B is at an angle with respect to the cross-section).

the distance between the surface and beam center was 200 μm (Fig. 4b), comparable to the penetration depth in pure magnesium of Cu Kα X-rays (70 μm) [47]. Exactly the same diffracting volume was identified before each measurement by radiography using a charge-coupled-device (CCD) camera, positioned far enough (about 600 mm) from the sample to allow for phase propagation (phase-enhanced imaging [43–46,48,49]). This volume contained one complete fiber (whose WB$_4$ fiber core is marked as B

in Fig. 4b), as well as parts of three more fibers (with cores outside the measured volume, marked as A, C and D in Fig. 4b). The beam size was 100×100 μm^2, corresponding to an estimated diffraction volume of 0.02 mm^3, very close to the surface as shown in Fig. 4b.

2.3. Lattice strain determination

As illustrated in the diffraction pattern of Fig. 3, all phases present were fine-grained and polycrystalline, leading to smooth diffraction rings, except for the Mg phase, which was more coarse-grained and thus showed slightly spotty diffraction rings. To determine the lattice strains from measured diffraction rings, an algorithm similar to those from Refs. [28,32,50,51] is used, which takes into account the whole diffraction rings. This algorithm is implemented using the program language MATLAB (available from www.mathworks.com) and consists of the following six steps. First, the beam center, detector tilt, and sample-to-detector distance ("calibration parameters") are determined with the software FIT2D [52,53] using CeO$_2$ (1 1 1) reflection near the detector center and CeO$_2$ (3 1 1) and (2 2 2) reflections near its outer edge. Second, the diffraction pattern is converted from polar to cartesian coordinates in N radial × M azimuthal bins (here $N = 750$, corresponding to 2.3 pixels, and $M = 144$, corresponding to an angle increment of 2.5°) using the calibration parameters to correct for beam center, detector tilt and sample-to-detector distance. Third, for selected diffraction peaks, the profile of the peak intensity as a function of radial distance is fitted using a pseudo-Voigt function to find the radial peak center R. This is done for all M azimuthal bins (i.e. in angle increments of $\eta = 2.5°$). Fourth, the $R(\eta)$ values are converted to absolute d-spacings $d(\eta)$ using the above calibration parameters, in addition to the known X-ray wavelength. Fifth, plots of R vs. $\sin^2(\psi)$ are created for all applied stresses, where $\psi = \eta\theta\cos(\eta)$ (with θ as the Bragg angle and $0 < \eta < \pi/2$ and similar relationships given in Almer et al. [50] for $\pi/2 < \eta < 2\pi$). The resulting lines intersect at an invariant "strain-free" value R_0 at an invariant azimuthal angle η_0. Finally, the X-ray lattice strain ε for a given $(h k l)$ reflection is calculated using:

$$\varepsilon(\eta) = \frac{R_0 - R(\eta)}{R_0} \tag{1}$$

These values are then used to determine the longitudinal and transverse strains in the sample coordinate system ($e_{11} = \varepsilon(90°)$ and $e_{22} = \varepsilon(0°)$), using equations derived by He and Smith [54] for two-dimensional detectors.

3. Results

3.1. Microstructure

Fig. 2a shows a polished cross-section of the composite used for mechanical tests which consists of 68 vol.% MgB$_2$ fibers, as determined by counting all fibers in the composite
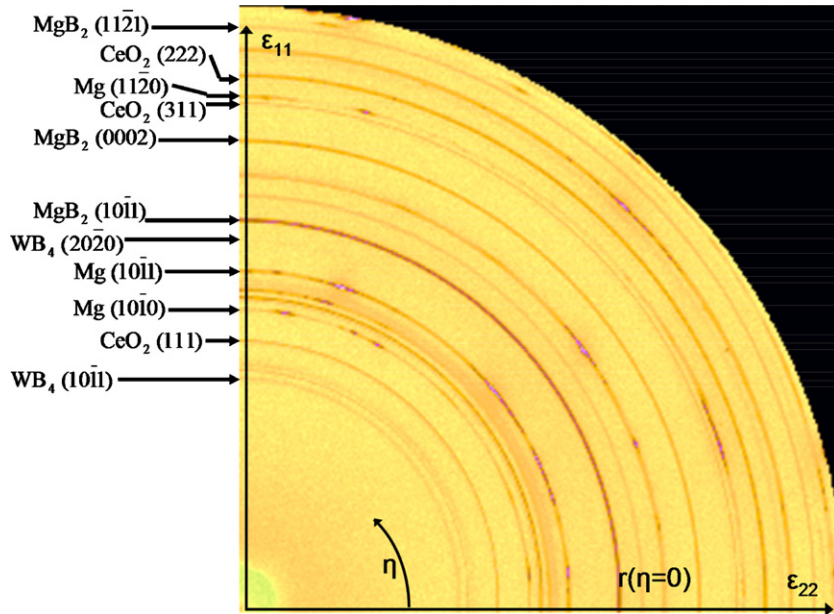
Fig. 3. Representative X-ray diffraction pattern (quarter of image plate) for Mg/MgB$_{2f}$ composite. All of the rings were identified as belonging to Mg, MgB$_2$, WB$_4$, and CeO$_2$, but for clarity only a subset is labeled.

cross-section of Fig. 2a and using their average diameter of 190 μm to determine their area fraction (the effect of fiber cracks is thus neglected). As reported in an earlier publication [14], the reacted fibers are nearly straight but exhibit substantial cracking, as expected from the large volume expansion associated with the B → MgB$_2$ conversion reaction. These cracks are illustrated in a scanning electron microscopy (SEM) image of a fiber, shown in Fig. 5, which was extracted by evaporating the Mg matrix in vacuum at 900 °C for 30 min. The 15 μm WB$_4$ fiber cores seem to remain intact and make up 0.4 vol.% of the composite, as calculated from the above fiber and core sizes (and again neglecting fiber cracks).

A radiographic image of a 1.02 mm thick cross-section of the composite is shown in Fig. 2b. Projections of individual MgB$_2$ fibers are visible as rounded regions, approximately 190 μm in diameter and slightly darker than the Mg matrix. In the center of each fiber, a near opaque region corresponds to the projection of the WB$_4$ cores. Most fibers are not exactly aligned in the longitudinal direction, so the projection of their cores appear as 15 μm thick lines, rather than as disks with 15 μm diameter (two examples are marked as A and B, respectively, in Fig. 2b). The projected length was measured for 53 fiber cores (out of a total of 482 cores within the Mg/MgB$_{2f}$ composite) from which the misorientation angle was calculated assuming that the cores were not bent. The average misorientation angle from the resulting angle distribution was 3.8°. This low value indicates that the fiber alignment was good, i.e. nearly all fibers were aligned parallel to the loading direction, as expected from the high fiber volume fraction. Good fiber alignment is also illustrated in Fig. 4a, which shows a radiographic projection of the composite perpendicular to the fiber axis.

In Fig. 4a, the small dashed square box indicates the diffraction beam size and the larger rectangular dashed box delineates the vertical scanning area which provides an average value for the lattice strains. Fig. 4b shows a similar radiograph of the near-surface region of the composite with the corresponding diffraction volume. It is apparent that the fiber orientation is not as good near the sample surface. Specific fiber cores in the diffraction beam are indicated in Fig. 4b. Cores A and B belong to fibers that are nearly perfectly aligned to the loading direction ($\theta \sim 0°$), while cores C and D belong to fibers with high misalignment ($\theta \sim 18°$).

3.2. Macroscopic composite stress–strain curve

The macroscopic stress–strain curve for the Mg/MgB$_{2f}$ composite is shown in Fig. 6. Upon compressive loading, elastic behavior with a Young's modulus of 121 GPa is observed up to the fourth applied stress level of −116 MPa. Upon further loading, plastic deformation takes place up to a maximum stress of −496 MPa and a total strain of −0.96%, corresponding to a plastic strain of −0.6%. At the three highest stresses, a small level of creep was recorded during the measurement time (the total creep strain was −0.017% for the highest applied stress of −496 MPa), which is not unexpected given the very high stresses as compared with the yield stress $\sigma_y = 21$ MPa for cast pure Mg [55]. Upon unloading, elastic behavior with a Young's modulus of 121 GPa occurs until the fourth unloading stress level of −132 MPa. Upon further unloading, reverse plasticity occurs, with a residual strain of −0.44% after complete unloading. No surface damage was visible upon visual inspection of the sample after testing.
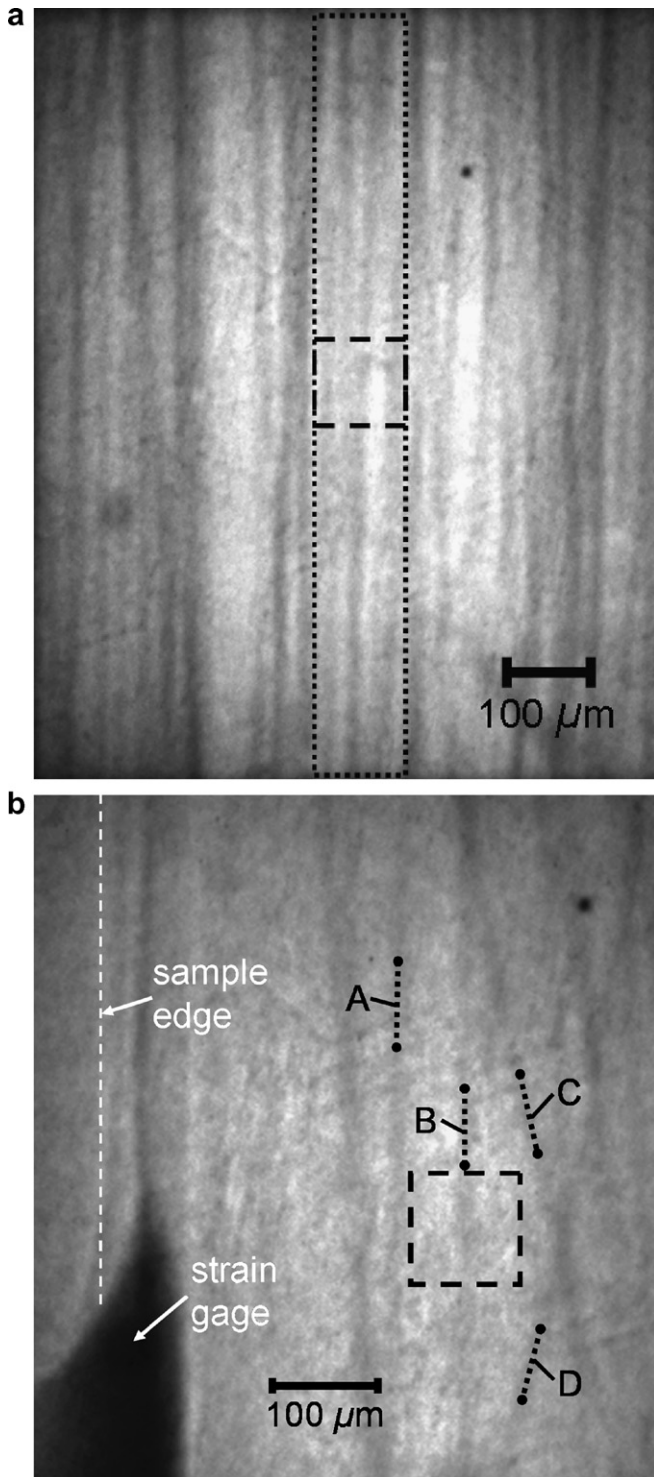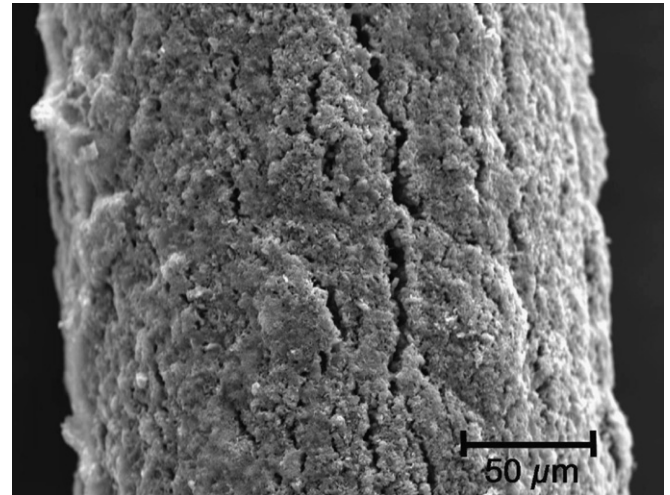
Fig. 5. SEM image of cracked MgB_2 fiber extracted from its matrix (fiber axis is near vertical).
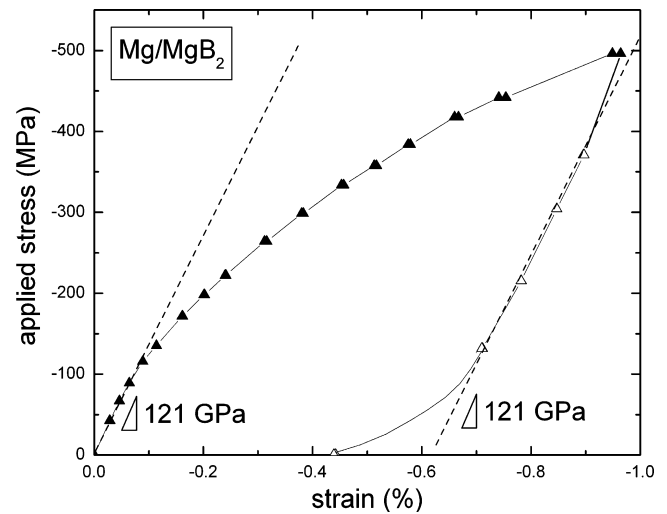

Fig. 6. Macroscopic stress–strain curve of Mg/MgB_{2f} composite with the dashed lines indicating the slopes of the elastic regions. Pairs of symbols at each stress levels, corresponding to start and end of diffraction measurement, are overlapping except at the highest stress due to creep.

Fig. 4. (a) Radiographic phase-enhanced image showing central region of the Mg/MgB_{2f} composite used for bulk strain measurements. Vertical dark lines are WB_4 fiber cores, and the load is applied vertically. The dashed box indicates the beam size ($100 \times 100 \ \mu m^2$). The dotted box indicates the diffracting region as the beam is scanned vertically over a height of 1 mm. (b) Radiographic phase-enhanced image showing circumferential region of the Mg/MgB_{2f} composite used for near-surface measurements. WB_4 fiber cores of fibers in the diffracting region (dotted box) are labeled by A, B, C and D, and are some of their length are indicated by dashed lines. Both A and B cores are nearly vertical (aligned to the loading direction with $\theta \sim 0°$), while C and D cores are highly misaligned ($\theta \sim 18°$).

3.3. Determination of lattice spacings and parameters

Fig. 7a and b shows plots of MgB_2 lattice strain and lattice spacing vs. $\sin^2\psi$ for various applied stresses. Each line was calculated from the average of the mean values of the four quadrants (0–90, 90–180, 180–270 and 270–360°) of azimuthal angles. Although only the $(10\bar{1}1)$ MgB_2 reflection is shown here, plots for various reflections from all three phases (Mg, MgB_2 and WB_4) were linear for all applied stresses in both loading and unloading.

The "strain-free" lattice spacings d_0 for the $(10\bar{1}1)$ MgB_2 reflection is illustrated in Fig. 7a and b. The Mg phase is coarser-grained, leading to spottier diffraction rings than the other phases present and, therefore, larger error in the determination of d_0. Since the WB_4 phase is less
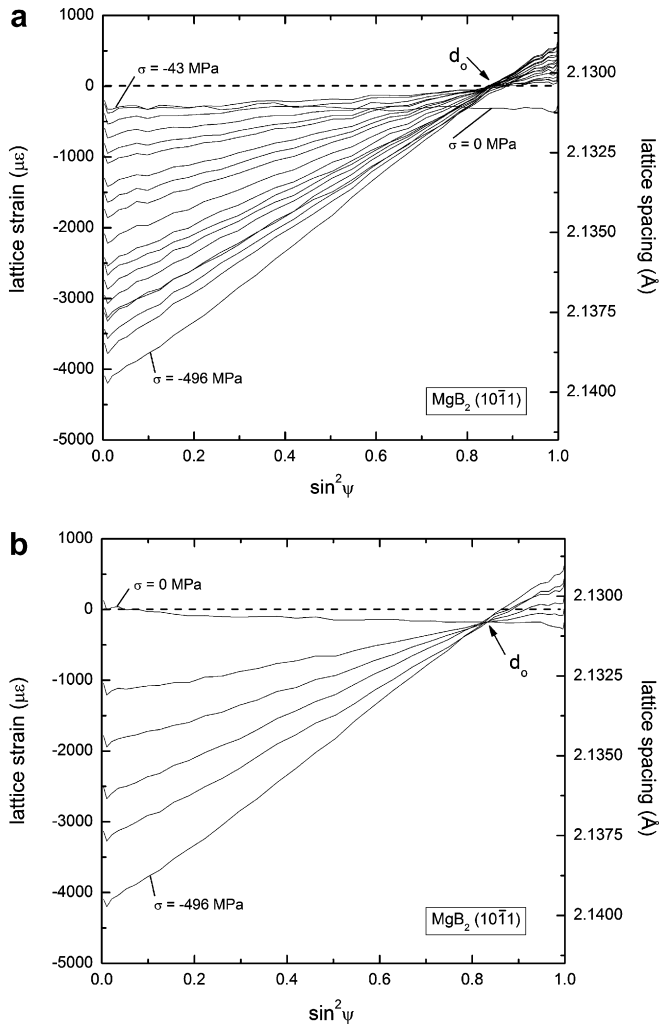
Fig. 7. Plots of lattice strain/lattice spacing vs. $\sin^2\psi$ for the MgB$_2$ ($10\bar{1}1$) reflection upon (a) loading and (b) unloading. Each line represents a single diffraction ring at a unique load.

Table 1
Lattice parameter values for the Mg, MgB$_2$ and WB$_4$ phases, as found in powder diffraction files (pdf) and as determined experimentally in the Mg/MgB$_{2f}$ composite studied here

Phase	Crystal structure	Lattice parameter (Å)		Source
		a	c	
Mg	Hexagonal	3.2094	5.2112	pdf# 35-0821
		3.215	5.213	Experimental
MgB$_2$	Hexagonal	3.0864	3.5215	pdf# 38-1369
		3.088	3.525	Experimental
WB$_4$	Hexagonal	5.200	6.340	pdf# 19-1373
		5.210	6.313	Experimental

and MgB$_2$ phases, they are slightly larger than, but probably within the experimental error of, the literature values also given in Table 1. For WB$_4$, the difference is larger: 0.2% expansion for a and 0.4% contraction for c.

Based on lattice parameters a and c for the MgB$_2$ phase, the density (ρ_{MgB_2}) for the MgB$_2$ phase is calculated from the following equation:

$$\rho_{MgB_2} = \frac{N \cdot MW_{MgB_2}}{N_A \cdot V} \tag{2}$$

where N is the number of atoms per unit cell ($N = 1$), N_A is Avogadro's number, MW_{MgB_2} is the molecular weight of MgB$_2$ ($MW_{MgB_2} = 45.93$ g mol^{-1}) and V is the volume of the unit cell (for a hexagonal system $V = a^2 c \sin(2\pi/3)$) [56]. Using this calculated density for MgB$_2$ ($\rho_{MgB_2} = 2.62$ g cm^{-3}) and the density for pure B ($\rho_B = 2.34$ g cm^{-3}) and their respective molecular weights, the volume expansion for the $2B \rightarrow MgB_2$ reaction is calculated as $v_{MgB_2}/2v_B = 1.90$, where v is the molar volume.

3.4. Lattice strain evolution during composite loading

3.4.1. General behavior

Plots of applied stress vs. elastic lattice strain are shown for the Mg ($10\bar{1}1$), MgB$_2$ ($10\bar{1}1$) and WB$_4$ ($10\bar{1}1$) reflections in the longitudinal direction (e_{11} parallel to the applied stress) in Fig. 8a and in the transverse direction (e_{22} perpendicular to the applied stress) in Fig. 8b. At zero applied load, residual longitudinal strains are small and tensile for the Mg and MgB$_2$ phases ($e_{11} = 300$ and 50 $\mu\varepsilon$) and very large and compressive for the WB$_4$ phase ($e_{11} = -2490$ $\mu\varepsilon$). Residual transverse strains are small for the Mg and MgB$_2$ phases ($e_{22} = -80$ and 30 $\mu\varepsilon$) and again very large but tensile for the WB$_4$ phase ($e_{22} = 1040$ $\mu\varepsilon$).

Upon mechanical loading at applied stresses where the composite macroscopic deformation is elastic (from 0 to -116 MPa, Fig. 6), the slopes of the plots of applied stress vs. longitudinal lattice strain in Fig. 8a for the Mg matrix (121 GPa), MgB$_2$ fibers (119 GPa) and the WB$_4$ fiber cores (121 GPa) are, within experimental error, equal to each other and to the macroscopic Young's modulus for the composite (121 GPa, Fig. 6). Similarly, these loading slopes

than 1 vol% of the total composite, the diffraction rings are weaker making the determination of d_0 more difficult than for the MgB$_2$ phase. The "strain-free" lattice spacing for the MgB$_2$ ($10\bar{1}1$) was 2.1312 Å at zero applied load, 2.1305 Å upon loading and 2.1308 Å upon unloading as shown in Fig. 7a and b. These slight shifts in absolute lattice parameter do not have a significant impact on the strains measured, since the relative variation in lattice parameter is of main interest. These shifts were observed in additional MgB$_2$ reflections (not presented here) but not for the other phases, and may be related to the extensive cracking present in the fibers, as discussed later.

The lattice parameters a and c for each phase (Mg, MgB$_2$, and WB$_4$) were determined iteratively by minimizing the lattice strain in the unloaded condition for multiple reflections (($h00$), ($hk0$) and (hkl)). For lattice parameter determinations, Miller indices (hkl) are used for convenience rather than Miller–Bravais indices ($hkil$). These experimental lattice parameter values for Mg, MgB$_2$ and WB$_4$ phases are listed in Table 1. For the two main Mg
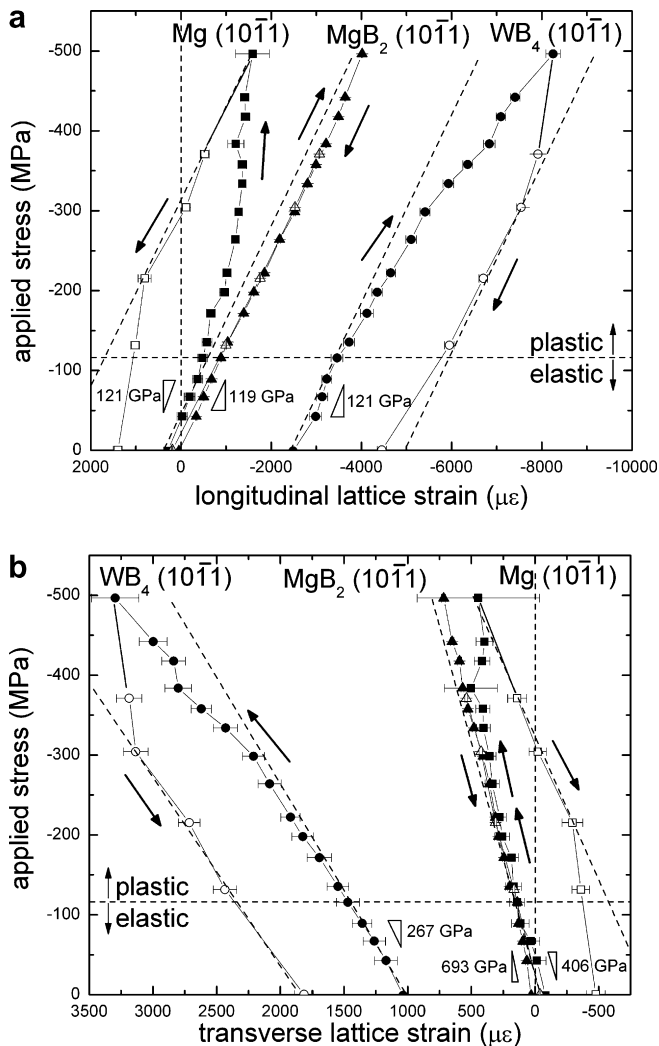
Fig. 8. Plots of applied compressive stress vs. (a) longitudinal and (b) transverse elastic lattice strain for Mg $(10\bar{1}1)$, MgB$_2$ $(10\bar{1}1)$ and WB$_4$ $(10\bar{1}1)$ reflections. Slope values are based on best fits of experimental data in the composite elastic range (with upper bound given by horizontal dashed line). Closed and open symbols represent loading and unloading (also shown with arrows), respectively.

in Fig. 8b for the transverse strains for the Mg matrix (−406 GPa) and MgB$_2$ fibers (−693 GPa) are approximately equivalent to each other, given the very large errors on the slopes, while the slope for the WB$_4$ fiber cores (−267 GPa) is significantly less steep. For the two main phases, Mg and MgB$_2$, the magnitude of the ratio of the transverse to longitudinal slopes (i.e. magnitude of e_{22}/e_{11} in the elastic range) provides the in situ Poisson's ratio, which takes values of 0.30 and 0.17, respectively. The value for Mg is in good agreement with the literature value of the Poisson's ratio for Mg ($v = 0.29$), indicating that the average state of stress of Mg phase is close to uniaxial compression. No value was found in the literature for the Poisson's ratio of MgB$_2$, but values well below those of the matrix are expected, given that Poisson's ratios of 0.09–0.12 have been reported for TiB$_2$, ZrB$_2$ and HfB$_2$ [57].

The onset of plasticity is visible in the macroscopic stress–strain curve (Fig. 6) at an applied stress of −116 MPa and also corresponds to a slight change in the slope for the longitudinal matrix strains in Fig. 8a for Mg $(10\bar{1}1)$. At applied stresses between −300 and −496 MPa, the matrix longitudinal strains become approximately constant (at about −1500 με), deviating sharply from the elastic line. An opposite deviation is observed for the WB$_4$ fiber cores, with lattice strains becoming larger than the elastic line. Similar deviations are also observed for the plots of transverse Mg and WB$_4$ strains (Fig. 8b). Such deviations from the elastic lines are usually associated in MMCs with load transfer occurring from a plastic matrix to elastic reinforcement, as discussed later. Here, however, the MgB$_2$ phase does not show any deviation with respect to the elastic slopes of the longitudinal or transverse strains (Fig. 8a and b).

Upon mechanical unloading, the slope of the Mg matrix plot in the longitudinal direction is 121 GPa, indicating a return to elastic behavior (Fig. 8a). When the applied stress has dropped to ca. −215 MPa, deviation from linearity is again observed, indicating reverse plasticity. The unloading plot for the WB$_4$ core phase also exhibits a mostly linear elastic behavior, within the large errors due to the small diffracting volume. Finally, upon unloading, the slope of the MgB$_2$ fiber phase plot remains constant and equal to the loading slopes, in both longitudinal and transverse directions (Fig. 8a and b). At the end of unloading, residual tensile strains for the Mg phase ($e_{11} = 1400$ με) and residual compressive strains ($e_{11} = -4450$ με) for the WB$_4$ phase are present in the longitudinal direction, while the MgB$_2$ phase is almost strain-free ($e_{11} = 200$ με). As shown in Fig. 8b, a symmetrical behavior is observed in the transverse direction to the applied stress (e_{22} large and positive for WB$_4$, smaller and negative for Mg, and near zero for MgB$_2$).

3.4.2. Anisotropy effects

The anisotropy in longitudinal strain response to the applied stress is shown for three Mg lattice reflections (($(10\bar{1}1)$, $(10\bar{1}0)$ and $(11\bar{2}0)$) in Fig. 9a, corresponding to three different sets of grains oriented with their respective crystallographic planes near perpendicular ($\eta = 90/270$) to the applied stress. In the elastic region, the slopes of loading plots for all three reflections are approximately equivalent to the Young's modulus of the Mg/MgB$_{2f}$ composite (121 GPa), indicating isotropic deformation. In the plastic region, however, a larger deflection from the elastic line (i.e. more load transfer) occurs for the Mg $(10\bar{1}1)$ reflection than for the Mg $(10\bar{1}0)$ and $(11\bar{2}0)$ reflections.

Similarly, the anisotropic response of three MgB$_2$ reflections (($(10\bar{1}1)$, (0002) and $(11\bar{2}1)$) is illustrated in Fig. 9b. Throughout loading, the applied stress–longitudinal lattice strain plots remain linear for all three MgB$_2$ reflections, indicative of elastic loading and no damage accumulation. The slopes for the MgB$_2$ $(10\bar{1}1)$ and (0002) reflections are approximately equivalent and equal
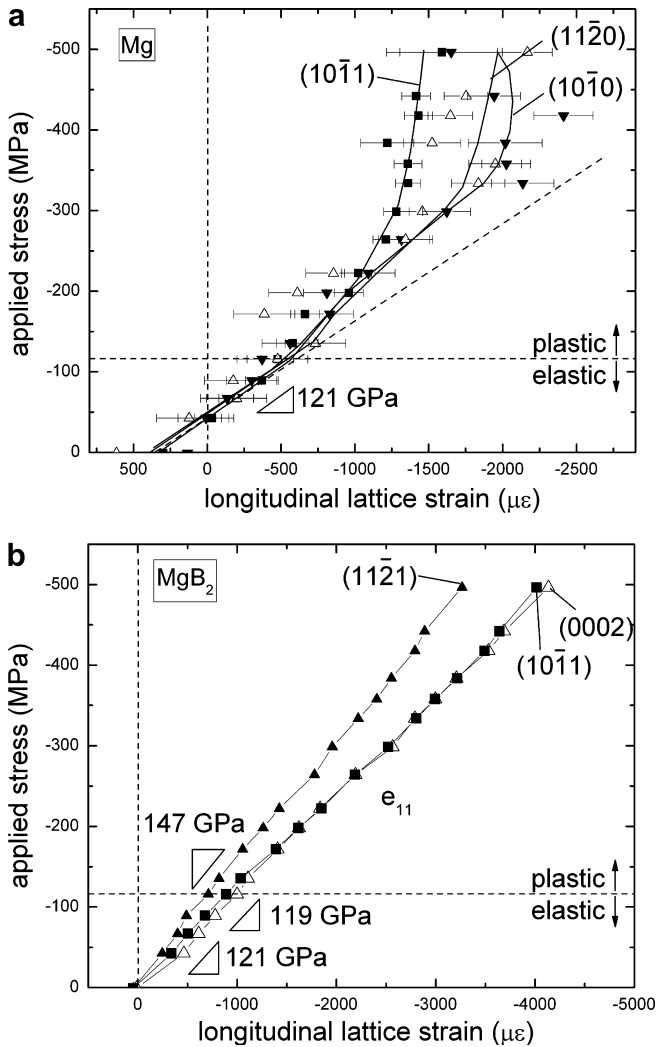
Fig. 9. Plots of applied compressive stress vs. longitudinal elastic lattice strain for (a) Mg $(10\bar{1}1)$, $(10\bar{1}0)$ and $(11\bar{2}0)$ reflections; and (b) MgB$_2$ $(10\bar{1}1)$, (0002) and $(11\bar{2}1)$ reflections on mechanical loading. Slope values are based on best fits of experimental data in the composite elastic range (with upper bound given by horizontal dashed line).

Fig. 10. Plots of applied compressive stress vs. longitudinal elastic lattice strain for (a) Mg $(10\bar{1}1)$ reflection and (b) MgB$_2$ $(10\bar{1}1)$ and WB$_4$ $(10\bar{1}1)$ reflections, shown for a bulk and a near-surface region on mechanical loading. Slope values are based on best fits of experimental data in the composite elastic range (with upper bound given by horizontal dashed line).

to the Young's modulus of the Mg/MgB$_{2f}$ composite (121 GPa), while the MgB$_2$ $(11\bar{2}1)$ reflection is stiffer (147 GPa); a similar effect is found for transverse strains (not shown).

Spatial anisotropy in mechanical response is illustrated in Fig. 10a for the Mg $(10\bar{1}1)$ longitudinal strains measured within the composite bulk and at a near-surface region. First, the residual strains are of opposite sign (300 µε in the bulk vs. −350 µε near the surface). Second, the slopes in the loading elastic range differ markedly (121 vs. 199 GPa). Third, the first onset of plasticity occurs at different stresses (−116 vs. −172 MPa). At higher stresses, however, both curves show strong deflection from the elastic line, indicating substantial load transfer from the matrix to the reinforcement. The larger error bars associated with the bulk measurements are due to the coarser grain size of the matrix in the core due to slower cooling rate, leading to spottier diffraction rings.
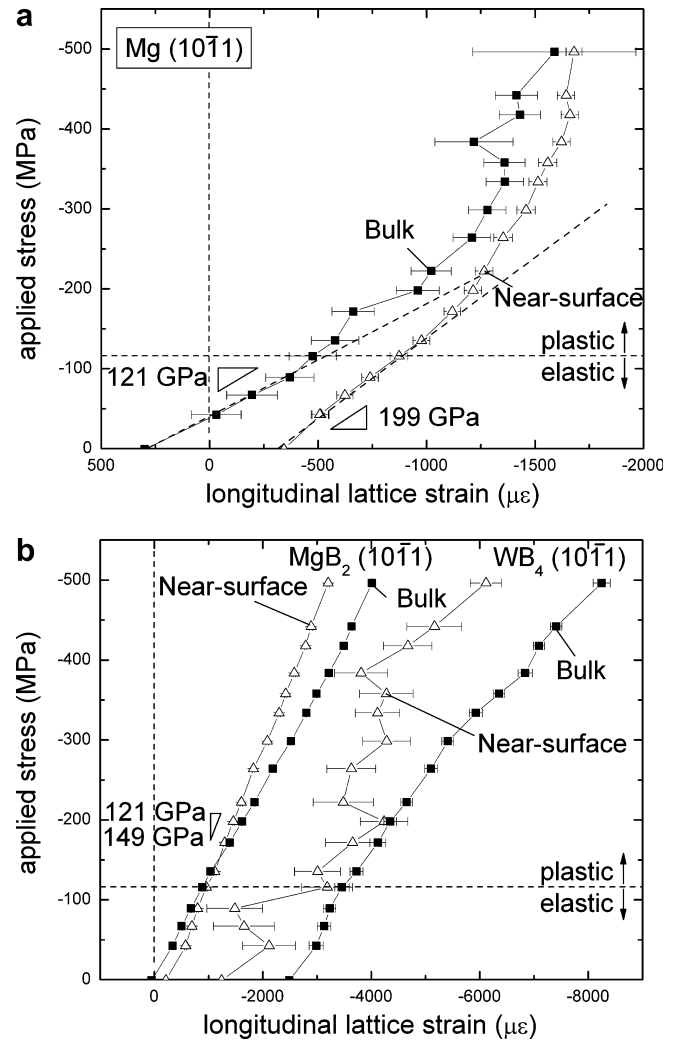
Similarly, differences between bulk and near-surface measurements are shown in Fig. 10b for the MgB$_2$ $(10\bar{1}1)$ reflection, for which the elastic slopes differ significantly (121 vs. 149 GPa). There are also visible differences for the WB$_4$ $(10\bar{1}1)$ reflection, but large errors are associated with the near-surface measurements which included a single fiber core with a very small diffraction volume (about 1.8×10^4 µm^3).

4. Discussion

4.1. Macroscopic composite elastic behavior

The longitudinal Young's modulus, E_{ROM}, of a composite containing perfectly aligned, uncracked fibers is given by the rule of mixture (ROM) equation:

$$E_{ROM} = V_{Mg}E_{Mg} + V_{MgB_2}E_{MgB_2} \tag{3}$$

where V is the volume fraction and E the Young's modulus. This equation predicts a value of $E_{ROM} = 199$ GPa for the present Mg/MgB$_{2f}$ composite, using matrix and fiber moduli of $E_{Mg} = 45$ GPa [56] and $E_{MgB_2} = 272$ GPa [58] (the WB$_4$ fiber core volume fraction is small enough that it can be neglected here). The experimentally measured value, $E_{comp} = 121$ GPa (Fig. 6), is, however, much lower. We consider two possibilities to explain this discrepancy: misaligned fibers and cracked fibers.

To estimate the effect of fiber misalignment, we use an equation for the Young's modulus (E_θ) of a composite with aligned fibers forming an angle θ with the applied stress [21]:

$$E_\theta = \left[\frac{m^4}{E_1} + \frac{n^4}{E_2} + \left(\frac{1}{G_6} - \frac{2v_1}{E_1} \right) m^2 n^2 \right]^{-1} \quad (4)$$

where $m = \cos\theta$, $n = \sin\theta$, E_1 is the ROM modulus in the longitudinal direction (Eq. (3)), $E_2 = (V_{Mg}/E_{Mg} + V_{MgB_2}/E_{MgB_2})^{-1}$ is the ROM modulus in the transverse direction, $G_6 = G_{Mg}/(1 - V_{Mg}^{1/2}(1 - G_{Mg}/G_{MgB_2}))$ is the ROM shear modulus, and $v_1 = V_{Mg}v_{Mg} + V_{MgB_2}v_{MgB_2}$ is the ROM Poisson ratio. Using the measured average fiber misorientation angle $\theta = 3.8°$, Eq. (4) predicts a Young's modulus of 198.5 GPa, very close to the value of 199 GPa calculated by the ROM equation (Eq. (3)) for fully aligned fibers. Even for an unrealistically high fiber misorientation angle $\theta = 15°$, Eq. (4) predicts a composite modulus of 187 GPa which remains much higher than the measured value $E_{comp} = 121$ GPa. This calculation provides only a rough estimation, since the fibers show a distribution of angles and are not parallel to each other, but it strongly suggests that fiber misorientation cannot explain the low stiffness of the composite.

The main cause for the Young's modulus discrepancy must thus be the cracks present in the MgB$_2$ fibers (Fig. 5). Introducing the measured value $E_{comp} = 121$ GPa for E_{ROM} in Eq. (1), the effective Young's modulus of the cracked MgB$_2$ fibers in the composite is found to be 157 GPa. This reduction by a factor 2.2 from the monolithic MgB$_2$ value of 272 GPa is credible in view of the very steep drops in stiffness observed in ceramics containing sharp cracks [59–62]: for instance, Wanner [59] measured a drop by a factor more than 20 in the Young's modulus of plasma-sprayed spinel with 13 vol.% slit-like cracks aligned perpendicular to the testing direction. The present MgB$_2$ fibers have a similarly high crack volume fraction of 4.2 vol.% (as determined from the cross-section of six fibers from another sample processed identically to the present one).

4.2. Residual elastic strains before composite loading

Similar to most other MMCs, the present Mg/MgB$_{2f}$ composite consists of matrix and reinforcement displaying a large mismatch in coefficients of thermal expansions: 26.6×10^{-6} K^{-1} for Mg [63], 5.4–6.4×10^{-6} K^{-1} in the

a-axis and 11.4–13.7×10^{-6} K^{-1} in the c-axis for MgB$_2$ [64,65] at ambient temperature. The value for WB$_4$ could not be found in the literature, but can be assumed to be lower than those of the lower-melting MgB$_2$. However, measured residual stresses between the two main phases of the composites, Mg and MgB$_2$, are small, indicating that relaxation by matrix plasticity occurred on cooling, first by creep (at high temperature) and then possibly by slip (at lower temperature). Thermal mismatch alone cannot explain the very large compressive residual strains in the WB$_4$ fiber cores ($e_{11} = -2490$ and $e_{11} = 1040$ με, Fig. 8a and b), corresponding to stresses of about -1.9 and 0.81 GPa, respectively, for a typical Young's modulus of 775 GPa (no value was found for WB$_4$, so we use here the modulus for W$_2$B$_5$ [57]).

Rather, these residual strains must arise during conversion of the W wires to WB$_4$ during the chemical vapor deposition synthesis of the B fiber, as described in Ref. [21], and/or during the subsequent reaction of B to MgB$_2$. This reaction leads to a large volume expansion of the fiber (calculated earlier to be 1.90), easily accounting for both the residual strains in the WB$_4$ core and the cracks in the MgB$_2$ fibers. The measured discrepancy in the lattice parameters (0.2% expansion for a and 0.4% contraction for c) are further evidence of the large residual strains in the WB$_4$ fiber cores. Nevertheless, they do not noticeably affect the residual strains in the other phases of the composites since the WB$_4$ volume fraction is so low.

4.3. Lattice strain evolution during composite loading

4.3.1. General behavior

In the elastic range for applied stresses between 0 and -116 MPa (Fig. 6), all three phases deform in an iso-strain manner, as illustrated by the fact that stress–lattice strain slopes are equal for each phase in both longitudinal and transverse directions, within experimental error (Figs. 8a, b and 9a, b). There is thus significant load transfer from the more compliant Mg matrix ($E_{Mg} = 45$ GPa) to the stiffer MgB$_2$ fibers ($E_{MgB_2} = 272$ or 157 GPa) and their WB$_4$ cores ($E_{WB_4} \approx 775$ GPa), indicating that the Mg/MgB$_2$ and MgB$_2$/WB$_4$ interfaces remain strongly bonded during elastic uniaxial compression.

Above the macroscopic yield stress of -116 MPa (Fig. 6), the stress–lattice strain slope for Mg increases for both longitudinal and transverse directions (Figs. 8a, b and 9a), first moderately in the stress range -116 to -300 MPa and then very markedly for stresses beyond -300 MPa, where the average slope is near infinity. This increase in slope indicates that, as the applied stress is raised, elastic strains (and stresses) do not increase in the Mg phase as rapidly as in the elastic range. This behavior is typical of matrix plasticity, as observed previously in many other MMCs [25,26,29,36,37,42,66], where it is explained by the large mismatch developing between the plastically deforming matrix surrounding the elastic reinforcement. In a two-phase composite without cracks, stress

equilibrium dictates that the applied stress–lattice strain slope for the reinforcement should decrease (i.e. that the reinforcement elastic strains and stresses increase more rapidly with applied stress than in the elastic range). This is indeed observed for the WB_4 phase in both e_{11} and e_{22} directions (Fig. 8a and b), but not for the MgB_2 phase, whose stress–lattice strain slopes remain linear and unchanged from the value measured in the elastic range. This indicates that the load shed by the plastic matrix is transferred to the WB_4 fiber core but not to the MgB_2 main fiber body.

This unexpected behavior is probably linked to the complex and extensive cracking of the MgB_2 fiber phase, and the fact that most of these cracks are filled with Mg matrix and extend to the WB_4 fiber cores. Also, the high value of composite strain of 0.96% (as compared with typical ceramic fracture strains) without composite failure is probably only possible because of the presence of these matrix-filled cracks. They can be expected to close during compressive deformation of the composite, expelling the plastic matrix without producing catastrophic failure of the fibers (the small, but measurable creep strain, <0.02%, observed to accumulate at the highest stresses may also be explained by this mechanism). We do not attempt here to calculate by finite-element modeling the evolution of load transfer occurring between the three phases in this complex deformation scenario, as it would necessitate many assumptions concerning the cracks (size, geometry, sharpness, orientation, spatial and size distribution, etc.) which are not experimentally accessible. Also, a large number of cracks within numerous fibers would need to be modeled to achieve statistically relevant results. This is not feasible with current laboratory computers and must thus remain beyond the scope of this paper.

During the mechanical unloading of the composite, the evolution of the phase elastic strains (Fig. 8a and b) is typical of a fiber-reinforced MMC: all phases display near linear stress–lattice strain behavior, with slopes similar to those on loading, indicating elastic behavior. The Mg matrix seems to exhibit reverse plasticity at low stresses on unloading for both e_{11} and e_{22} directions, which is also expected, given the large strains recovered on unloading (about 0.4% if the linear curve is extrapolated to zero stress for Mg longitudinal strains, which is much higher than the yield strain of pure Mg, estimated as $\sigma_y/E = 21$ MPa/45 GPa = 0.05%). This leads to significant residual strains in the Mg matrix after unloading, which seem to be partially balanced by higher residual strains in the WB_4 core. Here, too, the complex architecture of the composite (fibers with matrix-infiltrated cracks and stiff cores) is probably responsible for the lack of significant residual strains in the MgB_2 phase.

4.3.2. Anisotropy effects

The crystallographic anisotropy in lattice strain evolution shown in Fig. 9a has also been reported in studies of unreinforced Mg [67,68] and is responsible for the limited ductility of Mg [69] which exhibits less than five independent slip systems at ambient temperature [67,68]. Here, three Mg reflections $((10\bar{1}1)$, $(10\bar{1}0)$ and $(11\bar{2}0))$ are examined. As shown in Fig. 9a, load transfer occurs more strongly from grains with first-order pyramidal slip $((10\bar{1}1)$ reflection) than from those showing prismatic slip $((10\bar{1}0)$ reflection). Similar behavior was reported in a previous study of unreinforced Mg AZ31B alloy [67,68].

Spatial anisotropy is illustrated in Fig. 10a and b, where the micromechanical response (residual strain, elastic slope, plastic region) for all phases differs when measured in the composite bulk or in a near-surface region. This spatial anisotropy is likely due to the different state of stress near surfaces. Also contributing may be the higher fiber misalignment near surfaces, as illustrated by the two grossly misaligned fibers marked C and D in Fig. 4b, which are partially within the diffracting volume. Fig. 10a and b illustrates the importance, for uniaxially loaded fiber-reinforced composites, of measuring average strains within a large volume in the bulk of the sample (as performed by neutron and synchrotron X-ray techniques) rather than over a smaller volume located near a surface (as done for example with laboratory X-ray sources).

5. Conclusions

Synchrotron X-ray diffraction was used to study lattice strain evolution during compressive deformation of a composite consisting of an Mg matrix containing 68 vol.% of aligned MgB_2 fibers with small WB_4 cores. The following conclusions were reached:

1. Large residual stresses are present in the WB_4 fiber cores, and are attributed to the large volume expansion from the reaction of B to MgB_2 during processing. Small residual stresses also exist in both the Mg matrix and the MgB_2 fibers, indicating relaxation of thermal mismatch developed on cooling.
2. In the elastic range of the composite, the three phases show the same elastic strains at a given stress, indicating that load is transferred from the compliant Mg matrix to the stiffer MgB_2 fiber and their WB_4 cores, and that the matrix/fiber and fiber/core interfaces are well bonded.
3. In the plastic range of the composite (0–0.6% plastic strain), the matrix experiences lower strain than the other phases at a given stress. This is indicative of additional load transfer due to mismatch between the plastic matrix and the elastic reinforcement. The rate of load transfer with increasing stress remains constant for the MgB_2 fibers but increases for the WB_4 fiber cores as compared with the elastic range. This complex behavior is attributed to the presence of fiber cracks infiltrated with Mg matrix.
4. Microstructural anisotropic effects on load transfer occur among the Mg $(10\bar{1}1)$, $(10\bar{1}0)$ and $(11\bar{2}0)$ reflections in the plastic range and among the MgB_2 $(10\bar{1}1)$, (0002) and $(11\bar{2}1)$ reflections in both elastic and plastic ranges.

5. Comparison between strain measurements in the composite bulk and near-surface volumes indicate that near-surface measurements are not representative of the bulk composite behavior.

Acknowledgements

References

[1] Nagamatsu J, Nakagawa N, Muranaka T, Zenitani Y, Akimitsu J. Nature 2001;410:63.

[2] Larbalestier D, Gurevich A, Feldmann DM, Polyanskii A. High-T_c superconducting materials foe electric power applications. Nature 2001;414:368.

[3] Larbalestier DC, Cooley LD, Rikel MO, Polyanskii AA, Jiang J, Patnaik S, et al. Strongly linked current flow in polycrystalline forms of the superconductor MgB_2. Nature 2001;410:186.

[4] Kambara M, Hari Babu N, Sadki ES, Cooper JR, Minami H, Cardwell DA, et al. High intergranular critical currents in metallic MgB_2 superconductor. Supercond Sci Technol 2001;14:L5.

[5] Jin S, Mavoori H, Bower C, van Bower RB. High critical currents in iron-clad superconducting MgB_2 wires. Nature 2001;411:563.

[6] Grasso G, Malagoli A, Ferdeghini C, Roncallo S, Braccini V, Siri AS, et al. Large transport critical currents in unsintered MgB_2 superconducting tapes. Appl Phys Lett 2001;79:230.

[7] Kumakura H, Matsumoto A, Fujii H, Togano K. High transport critical current density obtained for powder-in-tube-processed MgB_2 tapes and wires using stainless steel and Cu–Ni tubes. Appl Phys Lett 2001;79:2435.

[8] Glowacki BA, Majoros M, Vickers M, Evetts JE, Shi Y, McDougall I. Superconductivity of powder-in-tube MgB_2 wires. Supercond Sci Technol 2001;14:193.

[9] Canfield PC, Finnemore DK, Bud'ko SL, Ostenson JE, Lapertot G, Cunningham CE, et al. Superconductivity in dense MgB_2 wires. Phys Rev Lett 2001;86:2423.

[10] Suo HL, Beneduce C, Dhalle M, Musolino N, Genoud JY, Flukiger R. Large transport critical currents in dense Fe- and Ni-clad MgB_2 superconducting tapes. Appl Phys Lett 2001;79:3116.

[11] Wang XL, Soltanian S, Horvat J, Liu AH, Qin MJ, Liu HK, et al. Very fast formation of superconducting MgB_2/Fe wires with high $J(c)$. Physica C 2001;361:149.

[12] Feng Y, Zhao Y, Pradhan AK, Zhou L, Zhang PX, Liu XH, et al. Fabrication and superconducting properties of MgB_2 composite wires by the PIT method. Supercond Sci Technol 2002;15:12.

[13] Fang H, Padmanabhan S, Zhou YX, Salama K. High critical current density in iron-clad MgB_2 tapes. Appl Phys Lett 2003;82:4113.

[14] DeFouw JD, Dunand DC. In situ synthesis of superconducting MgB_2 fibers within a magnesium matrix. Appl Phys Lett 2003;83:120.

[15] Dunand DC. Synthesis of superconducting Mg/MgB_2 composites. Appl Phys Lett 2001;79:4186.

[16] Marzik JV, Suplinskas RJ, Croft WJ, Moberly-Chan WJ, DeFouw JD, Dunand DC. The effect of dopant additions on the microstructure of boron fibers before and after reaction to MgB_2. In: Li J, Jansen M, Brese N, Kanatzidis M, editors. MRS symposium proceedings, vol. 848; 2005. p. FF6.2.1.

[17] Egilmez M, Ozyuzer L, Tanoglu M, Okur S, Kamer O, Oner Y. Electrical and mechanical properties of superconducting MgB_2/Mg metal matrix composites. Supercond Sci Technol 2006;19:359.

[18] Li Q, Gu GD, Zhu Y. High critical-current density in robust MgB_2/Mg nanocomposites. Appl Phys Lett 2003;82:2103.

[19] Giunchi G, Orecchia C, Malpezzi L, Masciocchi N. Analysis of the minority crystalline phases in bulk superconducting MgB_2 obtained by reactive liquid Mg infiltration. Physica C 2006;433:182.

[20] Chen YX, Li DX, Zhang GD. Microstructural studies of in situ formed MgB_2 phases in a Mg alloy matrix composite. Mater Sci Eng A 2002;337:222.

[21] Chawla KK. Composite materials. New York: Springer; 1998.

[22] Dunand DC, Mari D, Bourke MAM, Roberts JA. NiTi and NiTi–TiC composites. 4. Neutron diffraction study of twinning and shape-memory recovery. Metall Mater Trans A 1996;27:2820.

[23] Daymond MR, Lund C, Bourke MAM, Dunand DC. Elastic phase-strain distribution in a particulate-reinforced metal–matrix composite deforming by slip or creep. Metall Mater Trans A 1999;30:2989.

[24] Vaidyanathan R, Bourke MAM, Dunand DC. Phase fraction, texture and strain evolution in superelastic NiTi and NiTi–TiC composites investigated by neutron diffraction. Acta Mater 1999;47:3353.

[25] Hanan JC, Mahesh S, Ustundag E, Beyerlein IJ, Swift GA, Clausen B, et al. Strain evolution after fiber failure in a single-fiber metal matrix composite under cyclic loading. Mater Sci Eng A 2005;399:33.

[26] Clausen B, Bourke MAM, Brown DW, Ustundag E. Load sharing in tungsten fiber reinforced Kanthal composites. Mater Sci Eng A 2006;421:9.

[27] Clausen B, Lee SY, Ustundag E, Aydiner CC, Conner RD, Bourke MAM. Compressive yielding of tungsten fiber reinforced bulk metallic glass composites. Scripta Mater 2003;49:123.

[28] Wanner A, Dunand DC. Synchrotron X-ray study of bulk lattice strains in externally loaded Cu–Mo composites. Metall Mater Trans A 2000;31:2949.

[29] Maire E, Owen RA, Buffiere J-Y, Withers PJ. A synchrotron X-ray study of a Ti/SiCf composite during in situ straining. Acta Mater 2001;49:153.

[30] Balch DK, Ustundag E, Dunand DC. Elasto-plastic load transfer in bulk metallic glass composites containing ductile particles. Metall Mater Trans A 2003;34:1787.

[31] Balch DK, Dunand DC. Load partitioning in aluminum syntactic foams containing ceramic microspheres. Acta Mater 2006;54:1501.

[32] Young ML, Almer JD, Lienert U, Daymond MR, Haeffner DR, Dunand DC. Load partitioning between ferrite and cementite during elasto-plastic deformation of an ultrahigh-carbon steel. Acta Mater 2007; in press, doi:10.1016/j.actamat.2006.11.004.

[33] Maire E, Babout L, Buffiere J-Y, Fougeres R. Recent results on 3D characterisation of microstructure and damage of metal matrix composites and a metallic foam using X-ray tomography. Mater Sci Eng A 2001;319–321:216.

[34] Cloetens P, Pateyron-Salome M, Buffiere J-Y, Peix G, Baruchel J, Peyrin F, et al. Observation of microstructure and damage in materials by phase sensitive radiography and tomography. J Appl Phys 1997;81:5878.

[35] Stock SR. X-ray microtomography of materials. Inter Mater Rev 1999;44:141.

[36] MacDonald S, Preuss M, Maire E, Buffiere J-Y, Mummery PM, Withers PJ. X-ray tomographic imaging of Ti/SiC composites. J Microsc 2003;209:102.

[37] Preuss M, Withers PJ, Maire E, Buffiere J-Y. SiC single fibre full-fragmentation during straining in a Ti–6Al–4V matrix studied by synchrotron X-rays. Acta Mater 2002;50:3177.

[38] Blucher JT. J Mater Process Technol 1992;30:381.

[39] Balch DK, Ustundag E, Dunand DC. Diffraction strain measurements in a partially crystallized bulk metallic glass composite containing ductile particles. J Non-Cryst Solids 2003;317:176.

[40] Wanner A, Dunand DC. Methodological aspects of the high energy synchrotron X-ray diffraction technique for internal stress evaluation. J Neutron Res 2001;9:495.

[41] Haeffner DR, Almer JD, Lienert U. The use of high energy X-rays from the Advanced Photon Source to study stresses in materials. Mater Sci Eng A 2005;399:120.

[42] Hanan JC, Ustundag E, Beyerlein IJ, Swift GA, Almer JD, Lienert U, et al. Microscale damage evolution and stress redistribution in Ti–SiC fiber composites. Acta Mater 2003;51:4239.

[43] Cloetens P, Barrett R, Baruchel J, Guigay JP, Schlenker M. Phase objects in synchrotron radiation hard X-ray imaging. J Phys D 1996;29:133.

[44] Lee W-K, Fezzaa K, Wang J. Metrology of steel micronozzles using X-ray propagation-based phase-enhanced microimaging. Appl Phys Lett 2005;87.

[45] Stock SR, Ignatiev K, Dahl T, Barss J, Fezzaa K, Veis A, et al. Multiple microscopy modalities applied to a sea urchin tooth fragment. J Synchrotron Radiat 2003;10:393.

[46] Stock SR, Lee WK, Fezzaa K, Barss J, Dahl T, Veis A. X-ray absorption microtomography and phase contrast X-radiography of the structure of sea urchin teeth. J Bone Miner Res 2001;16:S443.

[47] Noyan IC, Cohen JB. Residual stress: measurement by diffraction and interpretation. New York: Springer; 1987.

[48] Raven C, Snigirev A, Snigireva I, Spanne P, Souvorov A, Kohn V. Phase-contrast microtomography with coherent high-energy synchrotron X-rays. Appl Phys Lett 1996;69:1826.

[49] Snigirev A, Snigireva I, Kohn V, Kuznetsov S, Schelokov I. On the possibilities of X-ray phase contrast microimaging by coherent high-energy synchrotron radiation. Rev Sci Instrum 1995;66:5486.

[50] Almer JD, Lienert U, Peng RL, Schlauer C, Oden M. J Appl Phys 2003;94:697.

[51] Korsunsky AM, Wells KE, Withers PJ. Mapping two-dimensional state of strain using synchroton X-ray diffraction. Scripta Mater 1998;39:1705.

[52] Hammersley AP. ESRF97HA02T, FIT2D: An introduction and overview. ESRF internal report; 1997.

[53] Hammersley AP. ESRF98HA01T, FIT2D V9.129 reference manual V3.1. ESRF internal report; 1998.

[54] He BB, Smith KL. In: SEM spring conference on experimental and applied mechanics and experimental/numerical mechanics in electronic packaging III, Houston, TX; 1998.

[55] Cubberly WH, editor. Metals handbook, vol. 2. Materials Park (OH): ASM International; 1990.

[56] Callister WD. Materials science and engineering. New York: Wiley; 2003.

[57] Schneider SJ, editor. Engineering materials handbook: ceramics and glasses. Materials Park (OH): ASM International; 1991.

[58] Nesterenko VF, Gu Y. Appl Phys Lett 2003;82:4104.

[59] Wanner A. Elastic modulus measurements of extremely porous ceramic materials by ultrasonic phase spectroscopy. Mater Sci Eng A 1998;248:35.

[60] Budinanski B, O'Connel RJ. Int J Solids Struct 1976;12:81.

[61] Kachanov M. On the effective moduli of solids with cavities and cracks. Int J Fract 1993;59:R17.

[62] Ramakrishnan N, Arunachalam VS. Effective elastic moduli of porous solids. J Mater Sci 1990;25:3930.

[63] Clyne TW, Withers PJ. An introduction to metal matrix composites. Cambridge: Cambridge University Press; 1993.

[64] Birkedal H, Van Beek W, Emerich H, Pattison P. Thermal expansion and phase purity of commercial MgB_2. J Mater Sci Lett 2003;22:1069.

[65] Jorgensen JD, Hinks DG, Short S. Lattice properties of MgB_2 versus temperature and pressure. Phys Rev B 2001:63.

[66] Sinclair R, Preuss M, Maire E, Buffiere J-Y, Bowen P, Withers PJ. The effect of fibre fractures in the bridging zone of fatigue cracked Ti–6Al–4V/SiC fibre composites. Acta Mater 2004;52:1423.

[67] Agnew SR, Duygulu O. Plastic anisotropy and the role of non-basal slip in magnesium alloy AZ31B. Int J Plasticity 2005;21:1161.

[68] Brown DW, Agnew SR, Bourke MAM, Holden TM, Vogel SC, Tome CN. Internal strain and texture evolution during deformation twinning in magnesium. Mater Sci Eng A 2005;399:1.

[69] Roberts CS. Magnesium and its alloys. New York: Wiley; 1960.